

pubs.acs.org/JCTC Article

Probing Delocalized Current Densities in Selenophene by Resonant X-ray Sum-Frequency Generation

Stefano M. Cavaletto and Shaul Mukamel*



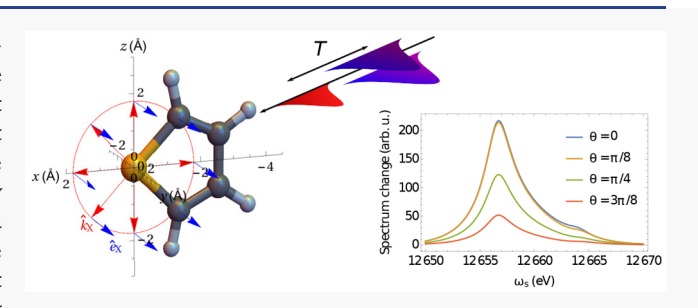
Cite This: https://dx.doi.org/10.1021/acs.jctc.0c00886



ACCESS

Metrics & More

ABSTRACT: Time-resolved, resonant X-ray sum-frequency generation in aligned selenophene molecules is calculated. A wave packet of valence-excited states, prepared by an extreme-ultraviolet pump pulse, is probed by two 12-keV X-ray probe pulses resonant with the Se core-excited states for variable time delays. At these hard-X-ray frequencies, the angström wavelength of the X-ray probe is comparable to the molecular size. We thus employ a nonlocal description of the light—matter interaction based on the minimal-coupling Hamiltonian. The wavevector-resolved resonant stimulated sum-frequency-generation signal, obtained by varying



Article Recommendations

the propagation direction of hard-X-ray pulses, can thus directly monitor the transition *current* densities between core and ground/valence states. This is in contrast to off-resonant diffraction, which detects the transition *charge* densities.

1. INTRODUCTION

Recent advances in the generation of bright, coherent X-ray pulses by high-order harmonic generation and free-electron lasers (FELs)² are enabling time- and space-resolved X-ray spectroscopy of molecules involving electronic core-excited states.³ Core electrons have element-specific transition energies and are strongly localized around a given atom. By tuning an X-ray pulse to a desired core, it is thus possible to monitor a specific region of the molecule.^{4,5} In recent experiments, X-ray FEL pulses have been used to directly access the evolution of the core-excited states⁶ or to generate a localized superposition of valence states via stimulated X-ray Raman scattering,^{7–9} for probing the charge migration of a superposition of electronic states in a molecule¹⁰ or the long-range charge and energy transfer in molecular aggregates.¹¹

The implementation of optical—X-ray wave mixing in multidimensional nonlinear X-ray spectroscopy constitutes a major challenge.³ Nonlinear wave mixing of infrared and visible pulses, such as sum-frequency generation (SFG), has long been applied to molecular vibrational spectroscopy.¹² The extension to X-ray frequencies was proposed in refs 13 and 14, but optical—X-ray SFG¹⁵ and optical—XUV four-wave mixing¹⁶ could only recently be demonstrated at FEL light sources.

Time-resolved X-ray sum-frequency diffraction $^{17-19}$ was recently put forward to access the evolution of the transition charge densities. In this $\chi^{(2)}$ process, a superposition of valence- 17,18 or core-excited states, 19 generated by a resonant XUV or X-ray pump pulse, respectively, is probed by two off-resonant X-ray pulses with time, frequency, and wavevector resolution. This is an SFG extension of time-resolved X-ray

diffraction, ^{20,21} which is currently applied for the reconstruction of time-dependent charge ^{22,23} and current densities. ^{24,25}

When the X-ray probe pulse is tuned to a core K-edge, time-resolved resonant X-ray SFG offers selectivity of valence dynamics via element-specific core transitions. In ref 26, resonant X-ray SFG in acetyl fluoride has been shown to provide selectivity by tuning an X-ray probe pulse to the F and O K-edges, thereby revealing which regions of the molecule contribute to the X-ray excitation. At those frequencies, which span a few hundreds of electronvolts, the X-ray pulse wavelength is long compared to the molecular size, and the signal does not depend on the propagation direction of the pulses.

Here, we investigate stimulated X-ray SFG in aligned selenophene molecules, using 12-keV X-ray probe pulses resonant with the Se core-excited states. Selenophene is a planar ring molecule, shown in Figure 1a, containing a Se atom with hard-X-ray core transitions. The associated X-ray wavelength $\lambda \sim 1$ Å is smaller than the molecular size, rendering the dipole approximation inapplicable and requiring a nonlocal description of the light—matter interaction based on the minimal-coupling interaction Hamiltonian. ^{27,28} Selenophene is thus a good candidate to probe delocalized molecular

Received: August 25, 2020



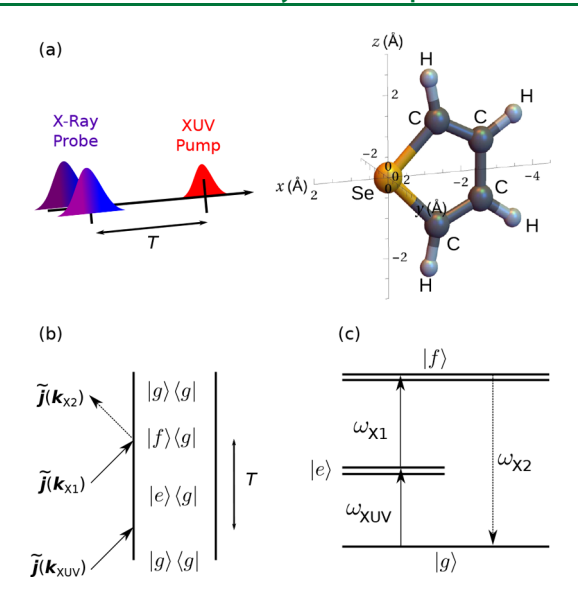


Figure 1. Stimulated X-ray sum-frequency-generation process. (a) Pulse configuration, with an XUV pump pulse and two X-ray probe pulses separated by a time delay T exciting aligned selenophene molecules at different propagation directions. (b) Ladder diagram: an eg coherence between the valence (e) and ground (g) states is generated by the XUV pump pulse, and a subsequent Raman transition is induced by the two X-ray probe pulses, with a resonant excitation of the core (f) states. A nonlocal description of the light—matter interaction captures the dependence of the X-ray excitation on the propagation direction of the X-ray probe pulses, $k_{\rm X1}$ and $k_{\rm X2}$, via the current-density $\tilde{j}(k)$. (c) Molecular level scheme, showing valence (e) and core (f) excitations.

current densities by nonlinear X-ray signals. In contrast to previous off-resonant^{17–19} and resonant²⁶ X-ray SFG studies, here, we investigate wavevector-resolved stimulated X-ray SFG for resonant, angström-wavelength pulses. By varying the X-ray probe propagation direction, we find observable changes in the SFG peak strengths, which can be ascribed to the spatial dependence of the transition current densities in the molecule. This allows one to experimentally reconstruct the space-dependent molecular X-ray couplings.

2. THEORETICAL MODEL

The stimulated X-ray SFG pulse configuration is displayed in Figure 1. A resonant XUV pump pulse prepares a superposition of valence-excited states, which is probed after a time delay T by two time-coincident resonant X-ray pulses, inducing a Raman transition from the valence states e to the ground state e via the core-excited states e. The SFG signal is obtained by detecting the spectrum of the transmitted X-ray pulse stimulating photon emission via the e0 transition. We assume plane-wave pulses with the associated vector potentials

$$\begin{aligned} \mathbf{A}_{\text{XUV}}(\mathbf{r}, t) &= \mathcal{A}_{\text{XUV}}(t + T) \mathrm{e}^{\mathrm{i}k_{\text{XUV}} \cdot \mathbf{r}} \mathrm{e}^{-\mathrm{i}\omega_{\text{XUV}}(t + T)} \hat{\mathbf{e}}_{\text{XUV}}, \\ \mathbf{A}_{\text{XI}}(\mathbf{r}, t) &= \mathcal{A}_{\text{XI}}(t) \mathrm{e}^{\mathrm{i}k_{\text{XI}} \cdot \mathbf{r}} \mathrm{e}^{-\mathrm{i}\omega_{\text{XI}} t} \hat{\mathbf{e}}_{\text{XI}}, \\ \mathbf{A}_{\text{X2}}(\mathbf{r}, t) &= \mathcal{A}_{\text{X2}}(t) \mathrm{e}^{\mathrm{i}k_{\text{X2}} \cdot \mathbf{r}} \mathrm{e}^{-\mathrm{i}\omega_{\text{X2}} t} \hat{\mathbf{e}}_{\text{X2}} \end{aligned}$$
(1)

with wavevectors k_{ij} carrier frequencies ω_{ij} polarization vectors \hat{e}_{ij} and envelope functions $\mathcal{A}_i(t)$, $i \in \{\text{XUV, X1, X2}\}$. We further define the Fourier transforms of $\mathcal{A}_i(t)$,

$$\tilde{\mathcal{A}}_{i}(\omega) = \int \mathrm{d}t \mathcal{A}_{i}(t) \mathrm{e}^{\mathrm{i}\omega t}$$
 (2)

which are centered on $\omega = 0$. Atomic units are used in the following, unless stated otherwise.

The stimulated SFG signal is calculated using the minimal-coupling radiation—matter interaction Hamiltonian^{27,28}

$$\hat{H}_{int}(t) = -\int d^3r \,\hat{\boldsymbol{j}}(\boldsymbol{r}) \cdot \boldsymbol{A}(\boldsymbol{r}, t)$$
(3)

where $\hat{j}(r)$ is the electronic current-density operator and A(r, t) $= A_{XIIV}(r, t) + A_{XI}(r, t) + A_{XI}(r, t)$ is the total vector potential. This nonlocal description, which avoids the multipole expansion of the light-matter interaction, fully accounts for the spatial variation of the short-wavelength X-ray pulses within the molecule. In eq 3, we assumed resonant excitations and thus neglected the contribution of the electronic chargedensity operator $\hat{\sigma}(r)$, which would be dominant for off-resonant excitations.²⁹ The stimulated SFG signal is obtained by measuring the spectrum of the transmitted X-ray pulse $A_{X2}(r, t)$, which stimulates the emission of a photon of frequency ω_s and propagation direction parallel to k_{x2} . The SFG signal $S(\omega_s)$ is defined and derived in Appendix A. For an optically thin medium, $N_{\text{mol}} S(\omega_s) d\omega_s$ represents the number of photons in the differential interval $[\omega_s, \omega_s + d\omega_s]$ of the X2 pulse which are absorbed due to its interaction with $N_{\rm mol}$ molecules. For an XUV pump pulse, the wavelength of which is significantly shorter than the molecular size and than the wavelength of the X-ray pulses X1 and X2, the phase-matching condition $k_{\text{XUV}} + k_{\text{X1}} = k_{\text{X2}}$ reduces to $k_{\text{X1}} \approx k_{\text{X2}} \doteq k_{\text{X}}$, implying that the two X-ray pulses are collinear. Because of their short wavelengths, which are comparable to the molecular size, the X-ray probe pulses can monitor the spatial dependence of the current density in the molecule, and the signal explicitly depends upon the propagation direction $k_{\rm X}$ via the transition current densities

$$\tilde{\mathbf{j}}_{ab}(\mathbf{k}) = \int \mathrm{d}^3 r \, \mathbf{j}_{ab}(\mathbf{r}) \mathrm{e}^{\mathrm{i}\mathbf{k}\cdot\mathbf{r}} \tag{4}$$

where the indices a and b in the matrix elements $A_{ab} = \langle a|\hat{A}|b\rangle$ run over the core and valence/ground states. For temporally well separated XUV pump and x-ray probe pulses, the signal reads

$$S(\omega_{s}, T, \mathbf{k}_{X}) = 2\mathbf{Im} \left\{ \sum_{e,f} \tilde{\mathcal{A}}_{X2}^{*}(\omega_{s} - \omega_{X2}) \right.$$

$$\times \tilde{\mathcal{A}}_{X1}(\omega_{s} - \omega_{eg} - \omega_{X1} + i\gamma_{e}) \frac{e^{-i\omega_{eg}T}e^{-\gamma_{e}T}}{-i(\omega_{s} - \omega_{fg} + i\gamma_{f})}$$

$$\times \tilde{\mathcal{A}}_{XUV}(\omega_{eg} - \omega_{XUV} - i\gamma_{e})$$

$$\times \tilde{\mathbf{j}}_{gf}(-\mathbf{k}_{X}) \cdot \hat{\mathbf{e}}_{X2}^{*} \tilde{\mathbf{j}}_{fe}(\mathbf{k}_{X}) \cdot \hat{\mathbf{e}}_{X1} \tilde{\mathbf{j}}_{eg}(\mathbf{k}_{XUV}) \cdot \hat{\mathbf{e}}_{XUV}$$
(5)

where we sum over the valence (e) and core (f) states, including the associated decay rates γ_e and γ_f and transition energies ω_{eg} and ω_{fg} to the ground state. For the XUV pulse, $\tilde{j}_{eg}(k_{\text{XUV}}) \approx j_{eg}(0)$, and the transition matrix elements reduce to the dipole couplings in the dipole approximation. We notice that modeling the X-ray probe pulses as plane waves with a well-defined value of $|k_{\text{X}}| = \omega_{\text{X}}/c$ is justified in our case, since the transition current densities $\tilde{j}_{ab}(k)$ depend on the

propagation direction k/|k| and do not vary appreciably with |k| within the X-ray pulse bandwidths.

The SFG signal strength is determined by the intensity of the X-ray probe pulses and the molecular density. Sufficiently low intensities are needed to realize the perturbative approach schematically shown in Figure 1b and to reduce the influence of competing effects, such as X-ray photoionization and population losses, which are not included here and can alter the molecular response $\langle \tilde{j}^{(-)}(r,t) \rangle$ in eq 18. While this restricts the range of utilizable X-ray intensities in an experiment, the SFG signal strength can still be maximized by a suitable choice of the molecular density. Optical-X-ray SFG¹⁵ and optical-XUV four-wave mixing 16 have been observed experimentally at FELs. Stimulated resonant X-ray Raman scattering, the process on which the proposed SFG setup relies, was successfully demonstrated in neon⁷ thanks to the amplification of the signal through the medium. In molecules, detecting signatures of stimulated Raman scattering in the transmitted X-ray pulse spectrum has proved challenging.³⁰ Stimulated X-ray Raman scattering was recently observed in NO molecules by measuring the resulting electronic population transfer with a second XUV pulse⁸ and not by directly detecting the absorbed photons. As we discuss in Appendix B, distinguishing the SFG signal in selenophene from the background spectrum of the Xray pulse is feasible, but may be challenging experimentally. However, this is expected to be enabled by ongoing progress in X-ray optics and technology, and the development of dedicated beamlines at FEL facilities.

In the following, we display the signal as a function of the frequency Ω conjugated to the delay T, by taking its Fourier transform

$$\tilde{S}(\omega_{s}, \Omega, \mathbf{k}_{X}) = \left| \int_{0}^{\infty} dT \ S(\omega_{s}, T, \mathbf{k}_{X}) e^{i\Omega T} \right|$$
 (6)

Since eq 5 was derived by assuming an XUV pump well separated from the X-ray probe pulses, the integral in eq 6 should formally exclude the short interval of time delays corresponding to overlapping pulses. This can be obtained experimentally at the postprocessing stage of the time-dependent signal $S(\omega_s)$, T, k_X). Including this short time-delay interval in eq 6 should have a negligible influence. For positive values of Ω , eq 6 reduces to

$$\tilde{S}(\omega_{s}, \Omega, \mathbf{k}_{X}) = 2 \left| \sum_{e,f} \tilde{\mathcal{A}}_{X2}^{*}(\omega_{s} - \omega_{X2}) \right| \\
\times \tilde{\mathcal{A}}_{X1}(\omega_{s} - \omega_{eg} - \omega_{X1} + i\gamma_{e}) \frac{1}{-i(\omega_{s} - \omega_{fg} + i\gamma_{f})} \\
\times \frac{1}{-i(\Omega - \omega_{eg} + i\gamma_{e})} \tilde{\mathcal{A}}_{XUV}(\omega_{eg} - \omega_{XUV} - i\gamma_{e}) \\
\times \tilde{J}_{gf}(-\mathbf{k}_{X}) \cdot \hat{\mathbf{e}}_{X2}^{*} \tilde{J}_{fe}(\mathbf{k}_{X}) \cdot \hat{\mathbf{e}}_{X1} \tilde{J}_{eg}(\mathbf{k}_{XUV}) \cdot \hat{\mathbf{e}}_{XUV} \right|$$
(7)

Scanning the time delay between the X-ray pulses X1 and X2 would probe the interpulse dynamics of the core states. However, this information is already provided by the frequency-resolved spectrum, the dependence of which on ω_s gives the energy and line width of the core states in the molecule. For this reason, we assumed time-coincident X-ray pulses.

3. SIMULATION RESULTS

3.1. Transition Energies and Current Densities of the Valence- and Core-Excited States in Selenophene. Different methods can be implemented to calculate valence- and core-excited states in molecules. Time-dependent density functional theory (TDDFT) is a practical method for large molecules. For smaller molecules such as selenophene, complete active space self-consistent field (CASSCF-)based methods provide higher precision with a reasonable computation cost. Here, we use CASSCF to calculate the lower valence- and Se core-excited states in selenophene. These are used to obtain the transition current densities $j_{ab}(r)$ and $\tilde{j}_{ab}(k)$ in eqs 4–7.

Valence- and core-excited states are calculated with the package MOLPRO. Valence states are calculated at the CASSCF(6/5)/cc-pVTZ level of theory, using a second-order Douglas–Kroll–Hess Hamiltonian in order to include relativistic corrections of the Se 1s electrons. The Se K-edge core-excited states are obtained by a restricted active space self-consistent field RASSCF(8/6)/cc-pVTZ calculation, by rotating the S(1s) orbital into the active space and restricting it to single occupancy. This provides the transition energies ω_{eg} and ω_{fg} of the valence- and core-excited states in the molecule, and the elements $D_{ab}^{\mu\nu}$ of the one-electron transition density matrix

$$D_{ab}^{\mu\nu} = \langle \Psi_a | \hat{b}_{\mu}^{\dagger} \hat{b}_{\nu} | \Psi_b \rangle \tag{8}$$

The indices a and b run over the ground, valence-, and core-excited states of the molecule, given by multiconfiguration self-consistent-field (MCSCF) wave functions $|\Psi_a\rangle$. μ and ν run over the single-electron orbitals $\chi_{\mu}(r)$, with associated creation and annihilation operators \hat{b}^{\dagger}_{μ} and \hat{b}_{μ} , respectively. The current-density operator can be written as

$$\hat{j} = \sum_{\mu,\nu} j_{\mu\nu}^{(1)} \hat{b}_{\mu}^{\dagger} \hat{b}_{\nu} \tag{9}$$

where $\hat{j}^{(1)}$ operates in the one-electron Hilbert space, with matrix elements

$$j_{\mu\nu}^{(1)}(\mathbf{r}) = \frac{1}{2} [\chi_{\mu}^{*}(\mathbf{r}) \nabla \chi_{\nu}(\mathbf{r}) - \chi_{\nu}^{*}(\mathbf{r}) \nabla \chi_{\mu}(\mathbf{r})]$$
(10)

The transition current densities in eqs 4-7 are finally given by

$$\mathbf{j}_{ab}(\mathbf{r}) = \sum_{\mu,\nu} D_{ab}^{\mu\nu} \mathbf{j}_{\mu\nu}^{(1)}(\mathbf{r})$$
(11)

3.2. Resonant X-ray SFG Signal of Aligned Selenophene. By tuning the X-ray probe pulses to different K-edges, resonant X-ray SFG offers selectivity of valence dynamics, revealing which valence-excited states couple to the element-specific core states for atoms localized at different points in the molecule. This provides indirect spatial information about the contributing molecular orbitals.

Here, this is demonstrated by tuning the X-ray probe pulses X1 and X2 to the Se K-edge in selenophene. We assume a broadband Gaussian XUV pump,

$$\begin{split} \mathcal{A}_{\text{XUV}}(t) &= \mathcal{A}_{\text{XUV},0} e^{-t^2/(2\tau_{\text{XUV}}^2)} \\ \tilde{\mathcal{A}}_{\text{XUV}}(\omega) &= \sqrt{2\pi} \, \tau_{\text{XUV}} \mathcal{A}_{\text{XUV},0} e^{-(\omega \tau_{\text{XUV}})^2/2} \end{split}$$

with duration $\tau_{\text{XUV}} = 200$ as, carrier frequency $\omega_{\text{XUV}} = 9$ eV, and linear polarization $\hat{e}_{\text{XUV}} = \hat{e}_z$ along the z direction. Such

broadband pulse generates a large superposition of valence states, even though this is not a requirement for the observation of signatures of delocalized current densities in the SFG signal. If needed, a broad superposition of valence states could also be produced by the stimulated Raman scattering of a broadband X-ray pulse. Alternatively, a narrower XUV pump pulse could be used to excite a few selected valence states of interest. The *eg* coherence generated by the pump is subsequently probed by the two broadband Gaussian X-ray pulses,

$$\mathcal{A}_{Xn}(t) = \mathcal{A}_{Xn,0} e^{-t^2/(2\tau_{Xn}^2)}$$

$$\tilde{\mathcal{A}}_{Xn}(\omega) = \sqrt{2\pi} \tau_{Xn} \mathcal{A}_{Xn,0} e^{-(\omega \tau_{Xn})^2/2}$$

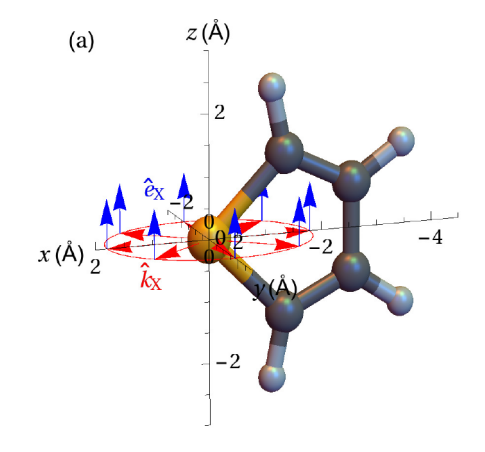
where $n \in \{1, 2\}$, both with duration $\tau_{Xn} = 100$ as and carrier frequencies $\omega_{X1} = 12.65$ keV and $\omega_{X2} = 12.66$ keV. Such broad 10 eV bandwidths, enabling the excitation of a large number of core states, are achievable with X-ray FELs, especially with recently demonstrated FEL attosecond pulses. The carrier frequencies used ensure that the X1 and X2 pulses are resonant with the fe and fg transitions, respectively. The peak strengths $\mathcal{A}_{XUV,0}$ and $\mathcal{A}_{Xn,0}$ act as multiplication constants in the signals of eqs 5 and 7. The spectra are displayed in arbitrary units in the following, and the experimental signal-to-background ratio is estimated in Appendix B.

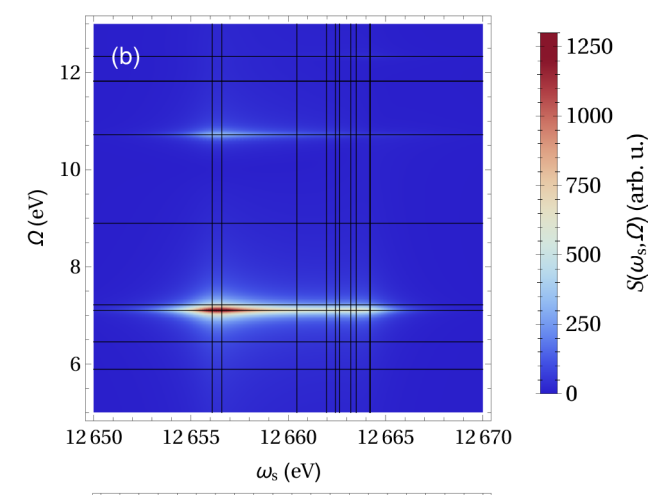
The transition energies ω_{eg} and ω_{fg} and the elements $D_{ab}^{\mu\nu}$ of the one-electron transition density matrix were obtained with CASSCF calculations. The lifetime broadening of the Se core-excited states is $\gamma_f = 1.16$ eV, 33 and we set $\gamma_e = 0.05$ eV for the valence-excited states. The two-dimensional SFG spectra shown in Figures 2 and 3 exhibit peaks along the Ω and ω_s axes, centered at the transition energies ω_{eg} and ω_{fg} , respectively, and revealing the couplings between the valence-and core-excited states involved in the Raman excitation process (see also eq 7). These couplings can be controlled by varying the propagation direction $k_{\rm X}$ of the X-ray probe pulses.

A first consequence of modifying the X-ray pulse propagation direction is the ensuing change of the polarization vectors $\hat{\boldsymbol{e}}_{Xn}$, which are perpendicular to \boldsymbol{k}_{Xn} and the directions of which vary when \boldsymbol{k}_{Xn} moves out of a given plane. The polarization vectors $\hat{\boldsymbol{e}}_{Xn}$ determine which components of $j_g(-\boldsymbol{k}_X)$ and $j_f(\boldsymbol{k}_X)$ in eq 7 contribute to the signal, with observable modifications in the SFG spectra.

Figure 2 depicts the SFG signal when the two X-ray pulses are linearly polarized along $\hat{e}_X = \hat{e}_z$, as shown in Figure 2a. The two-dimensional spectrum in Figure 2b was calculated for a propagation direction k_X along the x axis. The peaks along the x and x axis are centered on the transition energies x and x and x axis are centered on the transition energies x and x and x axis. The peaks along the x axis. The peaks along the x axis are centered on the transition energies x and x and x are specified, which are marked by the horizontal and vertical lines. The role of different Se core-excited states is highlighted in Figure 2c, which displays a section of the two-dimensional spectrum evaluated at the frequency x and x are clearly visible, centered at the frequencies x and x are clearly visible, centered at the frequencies x and x are x and x and x are x and x and x are specified even and x and x and x are specified state, x and x and x are specified even and x are x and x are x and x are x and x are x and x and x are x and x are x and x are x and x are x and x and x are x and

For linearly polarized X-ray pulses with $\hat{e}_X = \hat{e}_y$, as shown in Figure 3a, Figure 3b depicts the associated SFG spectrum evaluated for a propagation direction k_X along the x axis. As a result of different couplings, some of the peaks previously





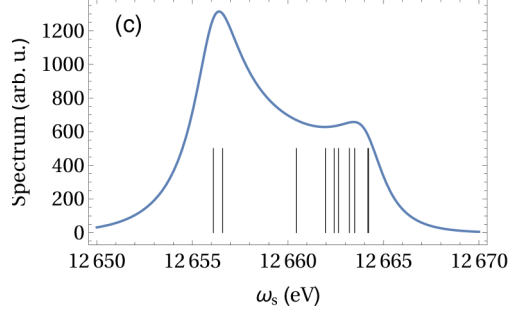


Figure 2. Resonant X-ray SFG of aligned selenophene molecules with X-ray pulses linearly polarized along the $\hat{e}_{\rm X}=\hat{e}_z$ direction. (a) Pulse geometry with the propagation direction $k_{\rm X}$ of the X-ray pulses varying in the xy plane, keeping a constant polarization vector $\hat{e}_{\rm X}=\hat{e}_z$. (b) X-ray SFG spectrum (eq 7) for broadband Gaussian XUV pump and X-ray probe pulses, with $\hat{e}_{\rm XUV}=\hat{e}_z$ and $k_{\rm X}$ along the x axis. The horizontal and vertical lines exhibit the transition energies ω_{eg} and ω_{fg} of the valence- and core-excited states in the molecule, respectively. (c) Slice of the X-ray SFG spectrum in panel b, evaluated at $\Omega=\omega_{e\chi g}=7.11$ eV. The vertical lines exhibit the transition energies ω_{fg} of the core-excited states.

visible in Figure 2b are now suppressed, such as those centered at $\Omega = \omega_{e,g} = 10.7$ eV or at $\omega_s = \omega_{f,g} = 12664$ eV. This is more clearly evinced by Figure 3c, where the section of the spectrum evaluated at $\Omega = \omega_{e,g} = 7.11$ eV shows a single main peak centered on $\omega_s = \omega_{f,g} = 12657$ eV.

3.3. Nonlocal Molecular Properties Accessed by Wavevector-Resolved Resonant X-ray SFG. When varying k_X within a given plane, holding the polarization vector fixed as

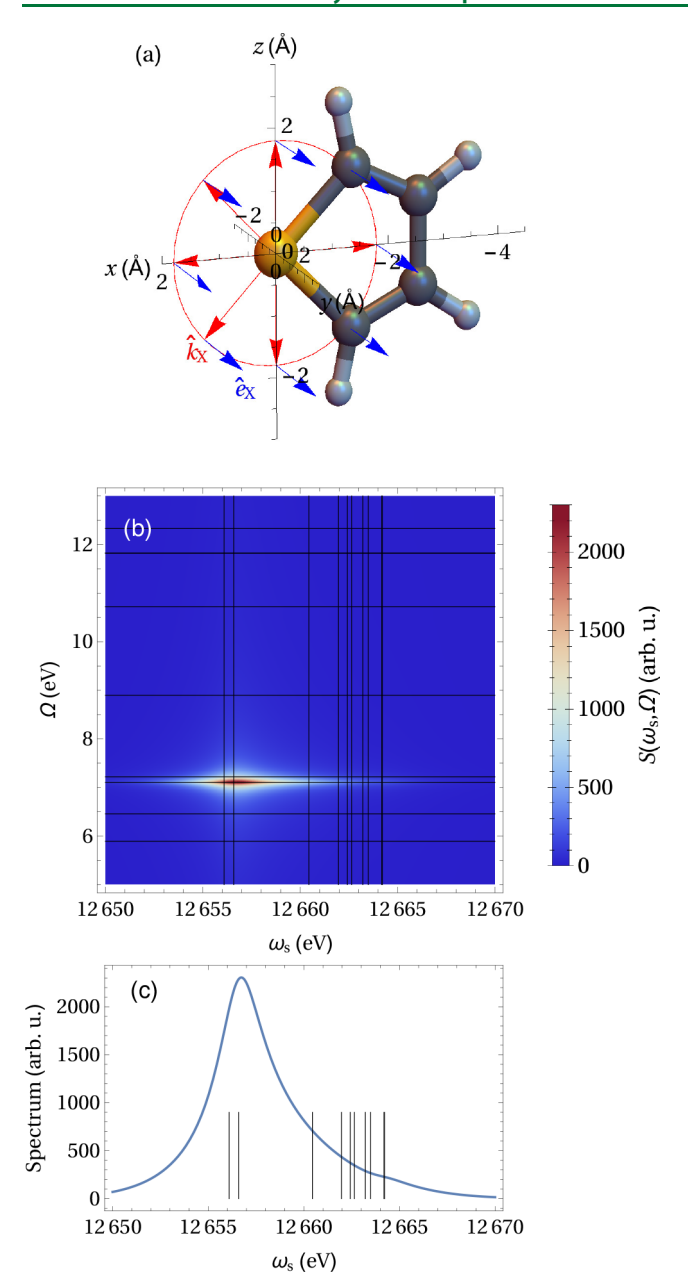
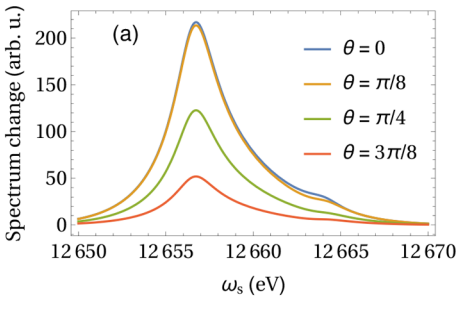


Figure 3. Resonant X-ray SFG of aligned selenophene molecules with X-ray pulses linearly polarized along the $\hat{e}_X = \hat{e}_y$ direction. (a) Pulse geometry with the propagation direction k_X of the X-ray pulses varying in the xz plane, keeping a constant polarization vector $\hat{e}_X = \hat{e}_y$. Panels b and c show the corresponding X-ray SFG spectra (eq 7) as in Figure 2b,c.

shown, for example, in Figures 2a and 3a, the dependence of $\tilde{j}_{gl}(-k_X)$ and $\tilde{j}_{fe}(k_X)$ on the X-ray pulse propagation direction produces observable variations in the resonant X-ray SFG signal. These arise from the short wavelength of the X-ray pulses, which renders them sensitive to spatial features within the molecule. Observing the dependence on the direction of k_X would require high-order multipoles and is readily captured by a nonlocal minimal-coupling formulation in terms of space-dependent current densities j(r).

In Figure 4, we depict the dependence of the main peak of Figure 3 on the X-ray pulse propagation direction. As shown in Figure 3a, we assume a wavevector $\mathbf{k}_X(\theta) = |\mathbf{k}_X|[\cos(\theta)\hat{\mathbf{e}}_x + \sin(\theta)\hat{\mathbf{e}}_z]$ rotating in the xz plane, with fixed polarization along



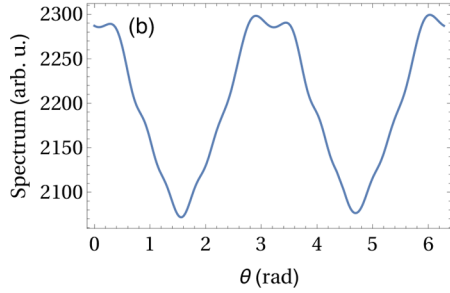


Figure 4. Resonant SFG spectrum for different propagation directions of the X-ray pulses, with $\hat{e}_{\text{XUV}} = \hat{e}_z$, $\hat{e}_{\text{X}} = \hat{e}_y$ and $k_{\text{X}}(\theta) = |k_{\text{X}}|[\cos(\theta)\hat{e}_x + \sin(\theta)\hat{e}_z]$ rotating in the xz plane. (a) Section of the X-ray SFG spectrum (eq 7) evaluated at $\Omega = \omega_{e_xg} = 7.11$ eV for different X-ray incident angles θ . The panel highlights the θ dependence of the signal by showing the difference between spectra evaluated at a given θ , as exhibited in the legend, and $\theta = \pi/2$. (b) X-ray SFG spectrum (eq 7) evaluated at $\Omega = \omega_{e_xg} = 7.11$ eV and $\omega_s = \omega_{f_zg} = 12657$ eV as a function of the X-ray incident angle θ .

 \hat{e}_y . The θ dependence of the peak in Figure 3c is highlighted in Figure 4a by displaying the difference between the spectrum evaluated at a given θ and at $\theta = \pi/2$. Figure 4a depicts sections of the spectra evaluated at $\Omega = \omega_{e,g} = 7.11$ eV for discrete values of θ , whereas Figure 4b presents the complete θ dependence of the peak at $\Omega = \omega_{e,g} = 7.11$ eV and $\omega_s = \omega_{f,g} = 12657$ eV. A significant change in the strength of this SFG peak is visible.

The peak in Figures 3 and 4 originates from the $g \rightarrow e_3 \rightarrow f_2$ \rightarrow g pathway associated with specific valence (e_3) and core (f_2) excited states. Figures 5 and 6 show the r and kdependence of the transition current densities involved in the above pathway. As visible in Figure 5a, the transition current density $j_{f,g}(r) \cdot \hat{e}_y$, with r lying in the xz plane, is mostly peaked at the Se site, where the resonant core-excited states are localized. Figure 5a also shows additional, weaker current densities at the C sites. Due to their short wavelengths, the probe X-ray pulses encounter a different current density depending on their propagation directions. This can be better observed in k space, as shown in Figure 5b. For a given $|k_x|$, the coupling due to an X-ray pulse in the $k_x k_z$ plane is determined by the transition current densities $\hat{j}_{f,g}(k)\cdot\hat{e}_{y}$ varying along the black circle in Figure 5b. Its dependence on the X-ray incident angle θ is displayed in Figure 5c.

Similar properties are featured by the transition current density $j_{f_2e_3}(r) \cdot \hat{e}_y$ between the valence- and core-excited states involved in the pathway, as apparent in Figure 6. Also in this case, the transition current density is mostly localized at the Se site, with additional contributions mostly around two of the four C sites. The associated transition current density $\tilde{j}_{f_2e_3}(k) \cdot \hat{e}_y$

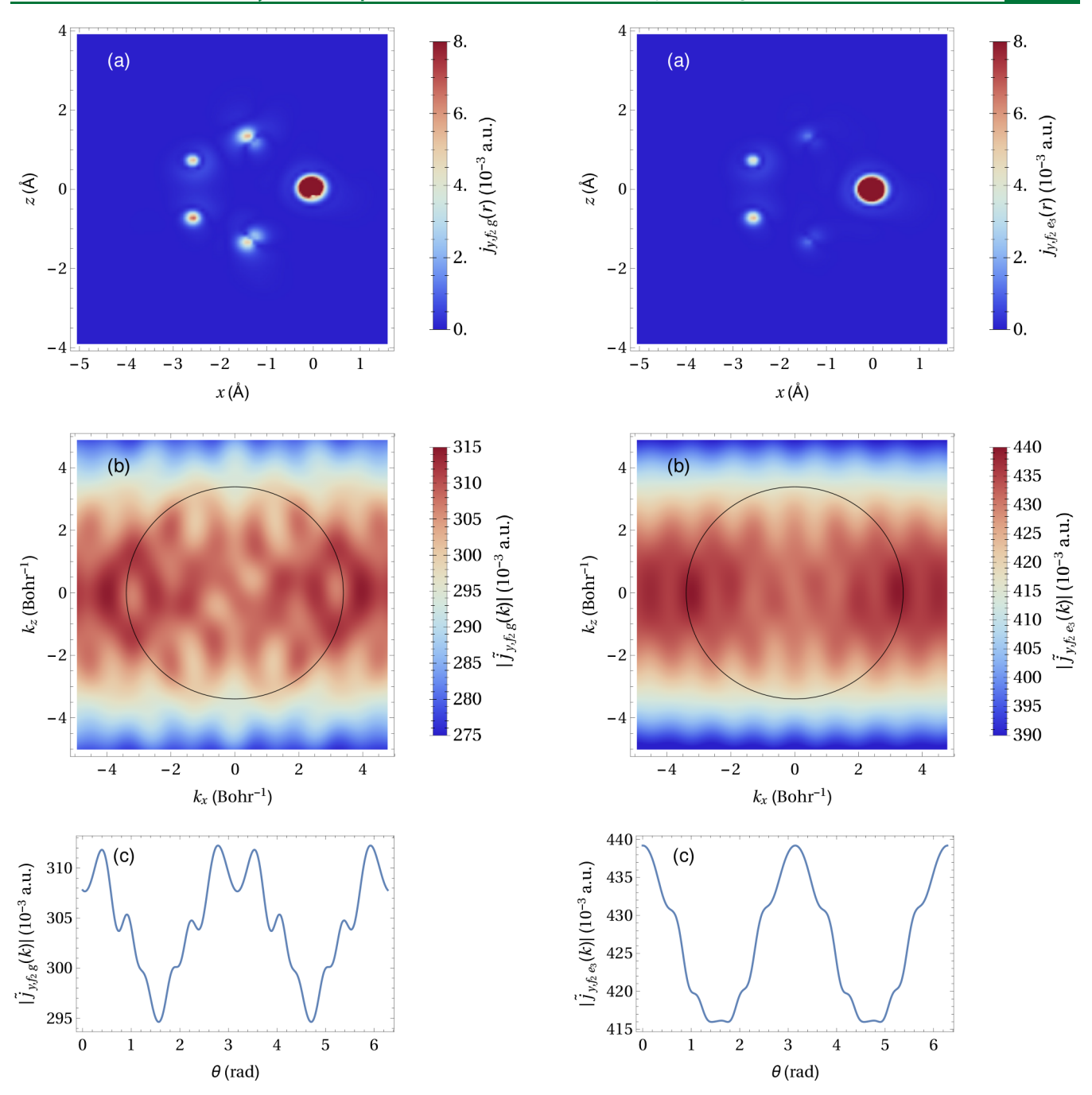


Figure 5. Transition current densities $j_{f,g}(r) \cdot \hat{e}_y$ and $\tilde{j}_{f,g}(k) \cdot \hat{e}_y$. (a) $|j_{f,g}(r) \cdot \hat{e}_y|$, for r lying on the xz plane. (b) Associated $|\tilde{j}_{f,g}(k) \cdot \hat{e}_y|$, for k lying on the $k_x k_z$ plane. By varying the X-ray propagation direction on such plane, $k_X(\theta) = |k_X| [\cos(\theta) \hat{e}_x + \sin(\theta) \hat{e}_z]$, the SFG signal is determined by the points lying on the black circle of radius $|k_X|$. (c) $|\tilde{j}_{f,g}(k) \cdot \hat{e}_y|$ for fixed $|k_X|$ and as a function of the X-ray incident angle θ .

in the $k_x k_z$ plane is shown in Figure 6b. Figure 6c depicts the dependence of $\tilde{j}_{f,e_2}(k) \cdot \hat{e}_v$ on the X-ray incident angle θ .

The spectra shown in Figures 3 and 4 are determined by the transition current densities involved in each step along the $g \rightarrow e_3 \rightarrow f_2 \rightarrow g$ pathway. Figure 7 displays the product of these three transition couplings: $\tilde{j}_{e,g}(k_{XUV})\cdot\hat{e}_z$, $\tilde{j}_{f_2e_3}(k_X(\theta))\cdot\hat{e}_y$, and $\tilde{j}_{gf_2}(-k_X(\theta))\cdot\hat{e}_y^*$. While the first dipole coupling due to XUV excitation is not sensitive to the spatial features of the molecule, the subsequent transition current densities are

Figure 6. Transition current densities $j_{f_2e_3}(r)\cdot\hat{e}_y$ and $\tilde{j}_{f_2e_3}(k)\cdot\hat{e}_y$. Panels a-c present the corresponding quantities as in Figure 5a-c.

clearly dependent on the incident angle θ of the X-ray pulses. The product of transition couplings in Figure 7 exhibits the same dependence on θ as the SFG spectrum in Figure 4b. This shows that wavevector-resolved resonant SFG can directly access nonlocal couplings and space-dependent transition current densities, when resonant X-ray pulses of short wavelength are used. This suggests interesting prospects for the direct reconstruction of space-dependent current densities in molecules.

4. DISCUSSION

Stimulated X-ray Raman excitations offer selectivity over electronic wave packets in molecules. By tuning X-ray pulses to

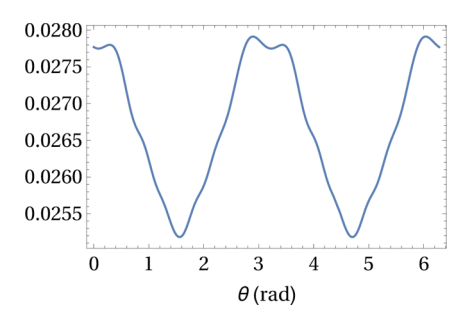


Figure 7. Modulus of the product of the transition current densities $|\tilde{\pmb{j}}_{g_{_{\! 2}}}(-\pmb{k}_{_{\! X}}(\theta))\cdot\hat{\pmb{e}}_{_{\! y}}^*\tilde{\pmb{j}}_{f_{_{\! 2}e_{_{\! 3}}}}(\pmb{k}_{_{\! X}}(\theta))\cdot\hat{\pmb{e}}_{_{\! y}}\,\tilde{\pmb{j}}_{e_{_{\! 2}g}}(\pmb{k}_{_{\! XUV}})\cdot\hat{\pmb{e}}_{_{\! z}}|$, which determines the spectra of Figures 3 and 4, with $\pmb{k}_{_{\! X}}(\theta)=|\pmb{k}_{_{\! X}}|[\cos(\theta)\hat{\pmb{e}}_{_{\! x}}+\sin(\theta)\hat{\pmb{e}}_{_{\! z}}]$ rotating in the xz plane.

the element-specific core transitions of different atoms in the molecule, the motion of the electronic charge between different points can be followed. For hard-X-ray transition energies such as for Se core-excited states, the short wavelength of the X-ray pulses can be comparable to the molecular size. In such a case, a multipolar expansion of the light—matter interaction Hamiltonian, in terms of electric and magnetic multipoles accounting for the global properties of the molecule, would require high-order multipoles. The interaction of the molecule with resonant X-ray pulses is fully characterized by the space-dependent current densities, which can be observed in the X-ray spectra.

We have employed a nonlocal-response formalism based on current-density operators and the minimal-coupling interaction Hamiltonian to calculate stimulated X-ray SFG of aligned selenophene molecules. Previous works had computed valence currents by monitoring the time-dependent charge densities.²⁵ The resonant hard-X-ray SFG signal directly provides the transition current densities involving the Se core. A stimulated X-ray Raman transition via Se core-excited states provides selectivity of valence-excited states. By varying the propagation direction of the X-ray pulses, while maintaining fixed polarization directions, we predicted observable changes in the strengths of the peaks of the SFG spectrum. These changes can be attibuted to the dependence of the corresponding core-valence and core-ground transition current densities on the propagation direction of the X-ray pulses. This effect originates from the short wavelength of the hard-X-ray pulses used, and may not be straightforwardly captured by expansion in multipoles.

The correspondence between the predicted spectrum in Figure 4b and the associated microscopic transition current densities in Figure 7 renders resonant SFG with hard-X-ray pulses a promising technique to directly access sections of the nonlocal transition current densities $\tilde{j}_{ab}(k)$. We notice that the technique, based on the interaction Hamiltonian in eq 3, requires resonant X-ray pulses, and can therefore span the transition current densities $\tilde{j}_{ab}(k)$ for $|k| = \omega_{\rm X}/c$, where $\omega_{\rm X}$ is tuned to the transition energy of the core-excited states.

For off-resonant pulses, the interaction Hamiltonian $\int \mathrm{d}^3 r \hat{\sigma}(r) |A(r,t)|^2$ provides direct access to the evolution of the transition charge densities $\sigma_{ab}(r)$. The nonlocal formalism can be extended to describe additional complex multidimensional techniques, involving sequences of resonant and off-resonant X-ray pulses, with properly set frequencies and delays. These can provide a more complete characterization of the charge dynamics in molecules.

APPENDIX A. DERIVATION OF THE SFG SIGNAL

The SFG signal is defined as the integrated rate of change of the number \hat{N}_s^{X2} of photons in a mode k_s with frequency ω_s^{34}

$$S(\omega_{\rm s}) = \int {\rm d}t \left\langle \frac{{\rm d}\hat{N}_{\rm s}^{X2}}{{\rm d}t} \right\rangle \tag{12}$$

For the heterodyne detection assumed here, the superscript X2 implies that the signal modes are restricted to those already occupied by the X-ray probe pulse $A_{\rm X2}(r,\,t)$. The photon-number rate of change is obtained by applying Heisenberg's equations of motion with the minimal-coupling interaction Hamiltonian in the rotating-wave approximation

$$\hat{H}_{int} = -\sum_{k,\lambda} \int d^3 r \left(\hat{\boldsymbol{j}}^{(+)}(\boldsymbol{r}) \cdot \boldsymbol{A}_{k,\lambda}(\boldsymbol{r}) \hat{a}_{k,\lambda} + \hat{\boldsymbol{j}}^{(-)}(\boldsymbol{r}) \cdot \boldsymbol{A}_{k,\lambda}(\boldsymbol{r}) \hat{a}_{k,\lambda}^{\dagger} \right)$$

$$(13)$$

Here, we define the positive- and negative-frequency contributions to the current density

$$\hat{j}(r) = \hat{j}^{(+)}(r) + \hat{j}^{(-)}(r)$$
(14)

and the vector-potential operator

$$\hat{A}(\mathbf{r}) = \sum_{\mathbf{k},\lambda} A_{\mathbf{k},\lambda}(\mathbf{r}) \hat{a}_{\mathbf{k},\lambda} + A_{\mathbf{k},\lambda}^*(\mathbf{r}) \hat{a}_{\mathbf{k},\lambda}^{\dagger}$$
(15)

We further denote the creation $(\hat{a}_{k,\lambda}^{\dagger})$ and annihilation $(\hat{a}_{k,\lambda})$ operators of a photon in a mode k and polarization \hat{e}_{k}^{λ} and the coefficient

$$A_{k,\lambda}(\mathbf{r}) = \sqrt{\frac{2\pi}{V_{\mathbf{q}}\omega_k}} e^{\mathbf{i}\mathbf{k}\cdot\mathbf{r}} \hat{e}_k^{\lambda}$$
(16)

for a field quantization volume V_q . This leads to

$$\frac{d\hat{N}_{s}^{X2}}{dt} = i \int d^{3}r \{\hat{\boldsymbol{j}}^{(-)}(\boldsymbol{r}) \cdot [\boldsymbol{A}_{s}^{X2}(\boldsymbol{r})]^{*} (\hat{a}_{s}^{X2})^{\dagger} - \text{H.c.}\}$$
 (17)

and the signal thus reads

$$S(\omega_{s}) = -2\operatorname{Im}\left\{\tilde{\mathcal{A}}_{X2}^{*}(\omega_{s} - \omega_{X2})\right.$$

$$\times \int dt \int d^{3}r \langle \hat{\boldsymbol{j}}^{(-)}(\boldsymbol{r}, t) \rangle \cdot \hat{\boldsymbol{e}}_{X2}^{*} e^{-ik_{X2} \cdot \boldsymbol{r}} e^{i\omega_{s} t} \right\}$$
(18)

where we have assumed that the X-ray pulse X2 is in a coherent state with expectation value

$$\langle \mathbf{A}_{\mathrm{s}}^{\mathrm{X2}}(\mathbf{r})\hat{a}_{\mathrm{s}}^{\mathrm{X2}}(t)\rangle = \tilde{\mathcal{A}}_{\mathrm{X2}}(\omega_{\mathrm{s}} - \omega_{\mathrm{X2}})\mathrm{e}^{\mathrm{i}\mathbf{k}_{\mathrm{X2}}\cdot\mathbf{r}}\mathrm{e}^{-\mathrm{i}\omega_{\mathrm{s}}t}\hat{\mathbf{e}}_{\mathrm{X2}}$$

given by the associated classical field.

The evolution of the current density $\langle \hat{j}^{(-)}(r,t) \rangle$ associated with the SFG diagram³⁵ in Figure 1b is obtained to second order in perturbation theory, including the interaction with the XUV pump and the first X-ray probe pulse:

$$\langle \hat{\boldsymbol{j}}^{(-)}(\boldsymbol{r},t) \rangle_{\text{SFG}} = (i)^2 \int_0^\infty dt_1 \int_0^\infty dt_2 \mathcal{A}_{\text{XI}}(t-t_2) e^{-i\omega_{\text{XI}}(t-t_2)}$$

$$\times \mathcal{A}_{\text{XUV}}(t-t_1-t_2+T) e^{-i\omega_{\text{XUV}}(t-t_1-t_2+T)}$$

$$\times \text{Tr} \left\{ \hat{\boldsymbol{j}}^{(-)}(\boldsymbol{r}) \hat{\boldsymbol{G}}(t_2) [\hat{\boldsymbol{j}}^{(+)}(\boldsymbol{k}_{\text{XI}}) \cdot \hat{\boldsymbol{e}}_{\text{XI}}] \hat{\boldsymbol{G}}(t_1) \right.$$

$$\times [\hat{\boldsymbol{j}}^{(+)}(\boldsymbol{k}_{\text{XUV}}) \cdot \hat{\boldsymbol{e}}_{\text{XUV}}] \hat{\rho}_0 \right\}$$

$$(19)$$

where we have defined the initial state of the system $\hat{\rho}_0 = |g\rangle\langle g|$, the operator

$$\hat{j}^{(+)}(k) = \int d^3r \, \hat{j}^{(+)}(r) e^{ik \cdot r}$$
 (20)

and the free-evolution operator $\hat{G}(t)$ which also includes the decay rates of the system. By inserting eq 19 into eq 18, and after performing the integrals in t_1 and t_2 explicitly assuming that the X-ray pulses do not overlap with the XUV pump pulse, we obtain the following sum-over-state expression for the signal:

$$S(\omega_{s}, T, \mathbf{k}_{X1}, \mathbf{k}_{X2}) = 2\operatorname{Im} \left\{ \sum_{e,f} \tilde{\mathcal{A}}_{X2}^{*}(\omega_{s} - \omega_{X2}) \right.$$

$$\times \tilde{\mathcal{A}}_{X1}(\omega_{s} - \omega_{eg} - \omega_{X1} + i\gamma_{e}) \frac{e^{-i\omega_{eg}T}e^{-\gamma_{e}T}}{-i(\omega_{s} - \omega_{fg} + i\gamma_{f})}$$

$$\times \tilde{\mathcal{A}}_{XUV}(\omega_{eg} - \omega_{XUV} - i\gamma_{e})$$

$$\times \tilde{\mathcal{J}}_{gf}(-\mathbf{k}_{X2}) \cdot \hat{\mathbf{e}}_{X2}^{*} \tilde{\mathcal{J}}_{fe}(\mathbf{k}_{X1}) \cdot \hat{\mathbf{e}}_{X1} \tilde{\mathcal{J}}_{eg}(\mathbf{k}_{XUV}) \cdot \hat{\mathbf{e}}_{XUV} \right\}$$

$$(21)$$

Since the XUV pump-pulse wavelength is significantly shorter than the molecular size and the wavelength of the X-ray pulses X1 and X2, eq 21 reduces to eq 5.

B. ESTIMATION OF THE SIGNAL-TO-BACKGROUND RATIO

The spectra in Figures 2 and 3 were displayed in arbitrary units. The signal-to-background ratio

$$R(\omega_{\rm s}) = \frac{8\pi\alpha n_{\rm mol} LS(\omega_{\rm s})}{\mathcal{R}_{\rm X2,0}^2 \tau_{\rm X2}^2 \omega_{\rm X2} e^{-(\omega_{\rm s} - \omega_{\rm X2})^2 \tau_{\rm X2}^2}}$$
(22)

can be estimated by comparing the number of absorbed photons $N_{\text{mol}} S(\omega_s) d\omega_s$ to the number of probe-pulse photons $A_{\text{foc}} \tilde{I}(\omega_s)/\omega_{\text{X2}} d\omega_s$ in the differential interval $d\omega_s$ centered on ω_s . n_{mol} is the density of molecules in the focal area A_{foc} and propagation length L, α the fine-structure constant, and

$$\tilde{I}(\omega_{\rm s}) = \frac{1}{8\pi\alpha} \frac{\omega_{\rm X2}^2 |\tilde{\mathcal{A}}_{\rm X2}(\omega_{\rm s} - \omega_{\rm X2})|^2}{2\pi}$$
(23)

the pulse spectral intensity.

We estimate the signal-to-background ratio for the peak in Figure 3b due to the $g \to e_3 \to f_2 \to g$ pathway. The associated transition current densities at fixed X-ray propagation directions are given by $|\tilde{j}_{gf_2}(-k_X)\cdot\hat{e}_{X2}^*| = 0.31$ au, $|\tilde{j}_{f_2e_3}(k_X)\cdot\hat{e}_{X2}^*|$ $\hat{\boldsymbol{e}}_{\text{XI}}|=0.44$ au, and $|\tilde{\boldsymbol{j}}_{e,g}(\boldsymbol{k}_{\text{XUV}})\cdot\hat{\boldsymbol{e}}_{\text{XUV}}|=0.21$ au, see also Figures 5 and 6. As predicted in Figure 4b, rotating the X-ray propagation direction in the xz plane causes a 10% change in the signal and in the signal-to-background ratio. We assume Xray probe pulses with peak intensities $|\mathcal{A}_{Xn,0}|^2 \omega_{Xn}^2/(8\pi\alpha) =$ $1.5 \times 10^{18} \text{ W/cm}^2$ and pulse durations $\tau_{Xn} = 100$ as, and an XUV pump with $|\mathcal{A}_{\text{XUV},0}|^2 \omega_{\text{XUV}}^2 / (8\pi\alpha) = 3.1 \times 10^9 \text{ W/cm}^2$ and τ_{XIIV} = 200 as: these peak intensities can be reached experimentally and are associated with Rabi frequencies j.A smaller than the associated line widths γ_e and γ_{θ} ensuring the validity of the perturbative approach employed here. From eq 5, the signal strength at the peak frequency $\omega_s = \omega_{f,g}$ can be estimated as

$$S \approx 2/\gamma_{f_{2}} \sqrt{2\pi} \tau_{X2} \mathcal{A}_{X2,0} |\tilde{\mathbf{j}}_{gf_{2}}(-\mathbf{k}_{X2}) \cdot \hat{\mathbf{e}}_{X2}^{*}| \sqrt{2\pi} \tau_{X1}$$

$$\mathcal{A}_{X1,0} |\tilde{\mathbf{j}}_{f_{2}e_{3}}(\mathbf{k}_{X1}) \cdot \hat{\mathbf{e}}_{X1}| \sqrt{2\pi} \tau_{XUV} \mathcal{A}_{XUV,0} |\tilde{\mathbf{j}}_{e_{3g}}(\mathbf{k}_{XUV}) \cdot \hat{\mathbf{e}}_{XUV}|$$
(24)

For a molecule density $n_{\rm mol} = 1.6 \times 10^{19}/{\rm cm}^3$ and a short propagation length of L=1 mm, eq 22 predicts a 0.27% signal-to-background ratio at the peak of the signal. Observing wavevector-dependent changes in this signal-to-background ratio is feasible, but may be challenging experimentally. Extended media can provide stronger signals, even though the detailed properties may be modified by propagation effects which were not accounted for here.

■ AUTHOR INFORMATION

Corresponding Author

Shaul Mukamel — Department of Chemistry and Department of Physics & Astronomy, University of California, Irvine, California 92697, United States; orcid.org/0000-0002-6015-3135; Email: smukamel@uci.edu

Author

Stefano M. Cavaletto — Department of Chemistry and Department of Physics & Astronomy, University of California, Irvine, California 92697, United States; orcid.org/0000-0003-1516-7519

Complete contact information is available at: https://pubs.acs.org/10.1021/acs.jctc.0c00886

Notes

The authors declare no competing financial interest.

ACKNOWLEDGMENTS

The support of the Chemical Sciences, Geosciences, and Biosciences division, Office of Basic Energy Sciences, Office of Science, U.S. Department of Energy through Award DE-FG02-04ER15571 and of the National Science Foundation (Grant CHE-1953045) is gratefully acknowledged. S.M.C. was partially supported by the DOE grant and gratefully acknowledges the support of the Alexander von Humboldt foundation through the Feodor Lynen program.

REFERENCES

- (1) Krausz, F.; Ivanov, M. Attosecond physics. Rev. Mod. Phys. 2009, 81. 163.
- (2) Pellegrini, C.; Marinelli, A.; Reiche, S. The physics of x-ray free-electron lasers. *Rev. Mod. Phys.* **2016**, *88*, 015006.
- (3) Bennett, K.; Zhang, Y.; Kowalewski, M.; Hua, W.; Mukamel, S. Multidimensional resonant nonlinear spectroscopy with coherent broadband x-ray pulses. *Phys. Scr.* **2016**, *T169*, 014002.
- (4) Schweigert, I. V.; Mukamel, S. Coherent ultrafast core-hole correlation spectroscopy: X-ray analogues of multidimensional NMR. *Phys. Rev. Lett.* **2007**, *99*, 163001.
- (5) Biggs, J. D.; Zhang, Y.; Healion, D.; Mukamel, S. Watching energy transfer in metalloporphyrin heterodimers using stimulated X-ray Raman spectroscopy. *Proc. Natl. Acad. Sci. U. S. A.* **2013**, *110*, 15597–15601.
- (6) Kanter, E. P.; Krassig, B.; Li, Y.; March, A. M.; Ho, P.; Rohringer, N.; Santra, R.; Southworth, S. H.; DiMauro, L. F.; Doumy, G.; Roedig, C. A.; Berrah, N.; Fang, L.; Hoener, M.; Bucksbaum, P. H.; Ghimire, S.; Reis, D. A.; Bozek, J. D.; Bostedt, C.; Messerschmidt, M.; Young, L. Unveiling and driving hidden resonances with high-fluence, high-intensity x-ray pulses. *Phys. Rev. Lett.* **2011**, *107*, 233001.

- (7) Weninger, C.; Purvis, M.; Ryan, D.; London, R. A.; Bozek, J. D.; Bostedt, C.; Graf, A.; Brown, G.; Rocca, J. J.; Rohringer, N. Stimulated electronic X-Ray Raman scattering. *Phys. Rev. Lett.* **2013**, *111*, 233902. (8) O'Neal, J. T.; Champenois, E. G.; Oberli, S.; Obaid, R.; Al-Haddad, A.; Barnard, J.; Berrah, N.; Coffee, R.; Duris, J.; Galinis, G.; Garratt, D.; Glownia, J. M.; Haxton, D.; Ho, P.; Li, S.; Li, X.; MacArthur, J.; Marangos, J. P; Natan, A.; Shivaram, N.; Slaughter, D. S.; Walter, P.; Wandel, S.; Young, L.; Bostedt, C.; Bucksbaum, P. H.; Picon, A.; Marinelli, A.; Cryan, J. P. Electronic population transfer via impulsive stimulated x-ray Raman scattering with attosecond soft-x-ray pulses. *Phys. Rev. Lett.* **2020**, *125*, 073203.
- (9) Rohringer, N. X-ray Raman scattering: a building block for nonlinear spectroscopy. *Philos. Trans. R. Soc., A* **2019**, 377, 20170471. (10) Worner, H. J.; Arrell, C. A.; Banerji, N.; Cannizzo, A.; Chergui, M.; Das, A. K.; Hamm, P.; Keller, U.; Kraus, P. M.; Liberatore, E.; Lopez-Tarifa, P.; Lucchini, M.; Meuwly, M.; Milne, C.; Moser, J.-E.; Rothlisberger, U.; Smolentsev, G.; Teuscher, J.; van Bokhoven, J. A.; Wenger, O. Charge migration and charge transfer in molecular systems. *Struct. Dyn.* **2017**, *4*, 061508.
- (11) Gray, H. B.; Winkler, J. R. Long-range electron transfer. *Proc. Natl. Acad. Sci. U. S. A.* **2005**, 102, 3534–3539.
- (12) Shen, Y. R. Surface properties probed by second-harmonic and sum-frequency generation. *Nature* **1989**, 337, 519–525.
- (13) Freund, I.; Levine, B. F. Optically Modulated X-Ray Diffraction. *Phys. Rev. Lett.* **1970**, *25*, 1241–1245.
- (14) Eisenberger, P.; McCall, S. L. X-Ray Parametric Conversion. *Phys. Rev. Lett.* **1971**, *26*, 684–688.
- (15) Glover, T. E.; Fritz, D. M.; Cammarata, M.; Allison, T. K.; Coh, S.; Feldkamp, J. M.; Lemke, H.; Zhu, D.; Feng, Y.; Coffee, R. N.; Fuchs, M.; Ghimire, S.; Chen, J.; Shwartz, S.; Reis, D. A.; Harris, S. E.; Hastings, J. B. X-ray and optical wave mixing. *Nature* **2012**, *488*, 603–608.
- (16) Bencivenga, F.; Cucini, R.; Capotondi, F.; Battistoni, A.; Mincigrucci, R.; Giangrisostomi, E.; Gessini, A.; Manfredda, M.; Nikolov, I. P.; Pedersoli, E.; Principi, E.; Svetina, C.; Parisse, P.; Casolari, F.; Danailov, M. B.; Kiskinova, M.; Masciovecchio, C. Fourwave mixing experiments with extreme ultraviolet transient gratings. *Nature* 2015, 520, 205–208.
- (17) Rouxel, J. R.; Kowalewski, M.; Bennett, K.; Mukamel, S. X-Ray Sum Frequency Diffraction for Direct Imaging of Ultrafast Electron Dynamics. *Phys. Rev. Lett.* **2018**, *120*, 243902.
- (18) Rouxel, J. R.; Kowalewski, M.; Mukamel, S. Diffraction-Detected Sum Frequency Generation: Novel Ultrafast X-ray Probe of Molecular Dynamics. *J. Phys. Chem. Lett.* **2018**, *9*, 3392–3396.
- (19) Cho, D.; Rouxel, J. R.; Kowalewski, M.; Lee, J.; Mukamel, S. Imaging of transition charge densities involving carbon core excitations by all X-ray sum-frequency generation. *Philos. Trans. R. Soc., A* **2019**, *377*, 20170470.
- (20) Bennett, K.; Kowalewski, M.; Rouxel, J. R.; Mukamel, S. Monitoring molecular nonadiabatic dynamics with femtosecond X-ray diffraction. *Proc. Natl. Acad. Sci. U. S. A.* **2018**, *115*, 6538–6547.
- (21) Parrish, R. M.; Martínez, T. J. Ab Initio Computation of Rotationally-Averaged Pump—Probe X-ray and Electron Diffraction Signals. *J. Chem. Theory Comput.* **2019**, *15*, 1523—1537.
- (22) Dixit, G.; Vendrell, O.; Santra, R. Imaging electronic quantum motion with light. *Proc. Natl. Acad. Sci. U. S. A.* **2012**, *109*, 11636–11640.
- (23) Glownia, J. M.; Natan, A.; Cryan, J. P.; Hartsock, R.; Kozina, M.; Minitti, M. P.; Nelson, S.; Robinson, J.; Sato, T.; van Driel, T.; Welch, G.; Weninger, C.; Zhu, D.; Bucksbaum, P. H. Self-referenced coherent diffraction x-ray movie of Ångstrom- and femtosecond-scale atomic motion. *Phys. Rev. Lett.* **2016**, *117*, 153003.
- (24) Popova-Gorelova, D.; Santra, R. Imaging instantaneous electron flow with ultrafast resonant x-ray scattering. *Phys. Rev. B: Condens. Matter Mater. Phys.* **2015**, *91*, 184303.
- (25) Hermann, G.; Pohl, V.; Dixit, G.; Tremblay, J. C. Probing Electronic Fluxes via Time-Resolved X-ray Scattering. *Phys. Rev. Lett.* **2020**, *124*, 013002.

I

- (26) Bruner, A.; Cavaletto, S. M.; Govind, N.; Mukamel, S. Resonant X-ray Sum-Frequency-Generation Spectroscopy of K-Edges in Acetyl Fluoride. *I. Chem. Theory Comput.* **2019**, *15*, 6832–6839.
- (27) Tanaka, S.; Chernyak, V.; Mukamel, S. Time-resolved X-ray spectroscopies: Nonlinear response functions and Liouville-space pathways. *Phys. Rev. A: At., Mol., Opt. Phys.* **2001**, *63*, 063405.
- (28) Rouxel, J. R.; Kowalewski, M.; Mukamel, S. Current vs charge density contributions to nonlinear X-ray spectroscopy. *J. Chem. Theory Comput.* **2016**, *12*, 3959–3968.
- (29) Cohen-Tannoudji, C.; Dupont-Roc, J.; Grynberg, G. Photons and Atoms-Introduction to Quantum Electrodynamics; Wiley: New York, NY, 1997.
- (30) Kimberg, V.; Rohringer, N. Stochastic stimulated electronic x-ray Raman spectroscopy. *Struct. Dyn.* **2016**, *3*, 034101.
- (31) Zhang, Y.; Hua, W.; Bennett, K.; Mukamel, S. In *Density-Functional Methods for Excited States. Topics in Current Chemistry*; Ferré, N., Filatov, M., Huix-Rotllant, M., Eds.; Springer: Cham, Switzerland, 2014; Vol. 368; pp 273–345.
- (32) Werner, H.-J.; Knowles, P. J.; Knizia, G. et al. *MOLPRO*, version 2019.2, *A package of ab initio programs*. Cardiff, UK, 2019; see https://www.molpro.net.
- (33) Krause, M. O.; Oliver, J. H. Natural widths of atomic K and L levels, $K\alpha$ X-ray lines and several KLL Auger lines. J. Phys. Chem. Ref. Data 1979, 8, 329–338.
- (34) Marx, C. A.; Harbola, U.; Mukamel, S. Nonlinear optical spectroscopy of single, few, and many molecules: Nonequilibrium Green's function QED approach. *Phys. Rev. A: At., Mol., Opt. Phys.* **2008**, 77, 022110.
- (35) Mukamel, S. Principles of nonlinear optical spectroscopy; Oxford University Press: New York, Oxford, 1995.